

Examination of the traditional Raman lidar technique.

II. Evaluating the ratios for water vapor and aerosols

David N. Whiteman

In a companion paper [Appl. Opt. **42**, 2571 (2003)] the temperature dependence of Raman scattering and its influence on the Raman and Rayleigh–Mie lidar equations were examined. New forms of the lidar equation were developed to account for this temperature sensitivity. Here those results are used to derive the temperature-dependent forms of the equations for the water-vapor mixing ratio, the aerosol scattering ratio, the aerosol backscatter coefficient, and the extinction-to-backscatter ratio. The error equations are developed, the influence of differential transmission is studied, and several laser sources are considered in the analysis. The results indicate that the temperature functions become significant when narrowband detection is used. Errors of 5% and more can be introduced into the water-vapor mixing ratio calculation at high altitudes, and errors larger than 10% are possible for calculations of aerosol scattering ratio and thus of aerosol backscatter coefficient and of extinction-to-backscatter ratio.

© 2003 Optical Society of America
OCIS codes: 010.3640, 010.3920.

1. Introduction

In part one of this paper¹ (hereafter referred to as part 1), a detailed examination of ways in which to evaluate Raman and Rayleigh–Mie lidar equations was presented. The details considered there included the effects of the temperature sensitivity of Raman scattering on both the Raman and the Rayleigh–Mie lidar equations, the calculation of atmospheric transmission, multiple scattering effects, and correction of photon pulse pileup. In this paper the ratios that lead to the meteorological quantities of water-vapor mixing ratio, aerosol scattering ratio and thus aerosol backscatter coefficient, and aerosol extinction-to-backscatter ratio are evaluated.

The structure of the paper is as follows: First the temperature-dependent forms of the Rayleigh–Mie and Raman lidar equations are reviewed. Then calculation of the water-vapor mixing ratio is discussed; this includes an examination of the altitude dependence of the temperature functions, development of the error equations, examination of differential transmission, and a discussion of calibration. The aerosol scattering ratio is then discussed

along with the appropriate error equations, and differential transmission is considered for several laser sources. The influence of narrowband detection on calculations of the aerosol backscattering coefficient is explored, and then the extinction-to-backscatter ratio is discussed.

2. Temperature-Dependent Rayleigh–Mie and Raman Lidar Equations

In part 1,¹ new forms of the lidar equation were derived that account for the influence of the temperature dependence of Raman rotational and vibrational–rotational scattering on the Rayleigh–Mie and Raman lidar equations. The final forms of these equations are repeated here for reference. Before proceeding, however, we review for clarity definitions given in part 1. The term “Rayleigh scattering” is used to signify the combination of Cabannes and rotational Raman scattering^{2,3} to recognize the fact^{2,3} that what Lord Rayleigh^{4,5} actually detected was a combination of elastic and rotational Raman scattering. The term “Mie scattering” is used to refer to scattering by particles of any shape, even though Mie theory⁶ pertains only to spherical particles. The term “Rayleigh–Mie lidar” is used to refer to systems that measure elastically scattered light from both molecules and particles of any shape as well as inelastically scattered pure rotational Raman scattering. Finally, although changes in transmission versus wavelength are due mostly to the characteristics of the interference filter or monochro-

The author (david.n.whiteman@nasa.gov) is with NASA/Goddard Space Flight Center, Greenbelt, Maryland 20771.

Received 28 January 2002; revised manuscript received 20 October 2002.

0003-6935/03/152593-16\$15.00/0

© 2003 Optical Society of America

mator used in a particular lidar channel, other optics in the system can also display wavelength-dependent transmission efficiency. Therefore the term “pass-band” will be used to describe the transmission function of a particular lidar optical channel.

Now, the single-scattering Rayleigh–Mie and Raman lidar equations for the background-subtracted power received by a detector as a function of range can be expressed as follows:

$$P(\Delta\lambda_R, r) = \frac{O_R(r) P_0(\lambda_L) A \xi(\lambda_L) [F_R(T) \beta_\pi^{\text{mol}}(\lambda_L, r) + \beta_\pi^{\text{aer}}(\lambda_L, r)]}{r^2} \exp \left[-2 \int_0^r \alpha(\lambda_L, r') dr' \right], \quad (1)$$

$$P(\Delta\lambda_X, r) = \frac{O_X(r) F_X(T) P_0(\lambda_L) A N_X(r) [d\sigma_X(\pi)/d\Omega] \xi(\lambda_X)}{r^2} \exp \left\{ - \int_0^r [\alpha(\lambda_L, r') + \alpha(\lambda_X, r')] dr' \right\}, \quad (2)$$

where $P(\lambda_R, r)$ is the backscattered power (after subtraction of any background contribution from, for example, skylight or detector noise and assuming single scattering) received at laser wavelength λ_L as a function of range r . $O_R(r)$ is the Rayleigh–Mie channel overlap function, $P_0(\lambda_L)$ is the output power of the laser at laser wavelength λ_L . $\beta_\pi^{\text{aer}}(\lambda_L, r)$ is the aerosol backscatter coefficient at the laser wavelength and at range r that is due to Mie scattering. $\xi(\lambda_L)$ is the total lidar receiver optical efficiency at the laser wavelength and includes factors such as the reflectivity of the telescope, the transmission of conditioning optics, the transmission of any filters, and the quantum efficiency of the detector. A is the receiver-telescope area. The exponential factor gives the two-way atmospheric transmission, where $\alpha(\lambda_L, r)$ is the total extinction coefficient at the laser wavelength that is due to scattering and absorption by molecules, particles, and any other atmospheric constituents such as water droplets and ice crystals as a function of range along the path of the laser beam. $\beta_\pi^{\text{mol}}(\lambda_L, r) = N_R(r) d\sigma_R(\pi)/d\Omega$, and $d\sigma_R(\pi)/d\Omega$ is the full Rayleigh cross section including the effects of rotational Raman scattering. Notice that in the Rayleigh–Mie equation the temperature-dependent term $F_R(T)$ multiplies only $\beta_\pi^{\text{mol}}(\lambda_L, r)$ and not $\beta_\pi^{\text{aer}}(\lambda_L, r)$ because only the molecular component of the signal exhibits the temperature dependence considered here.

The terms used in the Raman lidar equation are defined similarly, except that the atmospheric transmission term now involves both the outgoing wavelength of the laser and the return Raman-shifted wavelength. Furthermore, in the Raman lidar equation there is no aerosol backscatter term, so the temperature-dependent function multiplies the entire equation. This difference will become important in Section 4, where the aerosol scattering ratio is considered.

The temperature-dependent functions are defined by

$$F_X(T) = \frac{\int_{\Delta\lambda_X} [d\sigma_X(\lambda', \pi, T)/d\Omega] \xi(\lambda') d\lambda'}{[d\sigma_X(\pi)/d\Omega] \xi(\lambda_X)}, \quad (3)$$

where X refers to either Rayleigh scattering (in which

case rotational Raman lines carry the temperature dependence) or to a Raman vibrational mode from molecular species X . $\xi(\lambda)$ is the lidar system’s transmission efficiency as a function of wavelength. The interval $\Delta\lambda_X$ is that over which the lidar system has significant transmission for feature X . $F_X(T)[d\sigma_X(\pi)/d\Omega]$ may be interpreted as the effective molecular cross section consistent with the use of a monochromatic optical efficiency term, $\xi(\lambda_X)$, in the lidar equation. These forms of the lidar equations will be used in the derivations to come, after the calculation of the transmission terms in the lidar equations is carefully considered.

3. Water-Vapor Mixing Ratio

A. Definition

Water vapor is one of the most important atmospheric state variables. The profile of atmospheric water vapor strongly influences convective stability, which determines the likelihood of storm initiation. It also is the most active greenhouse gas because it absorbs terrestrial radiation more strongly than does CO_2 . The ratio of the mass of water vapor to the mass of dry air in a given volume, known as the water-vapor mixing ratio, is a convenient measure of the amount of water vapor in the atmosphere. The mixing ratio is conserved in atmospheric processes that do not involve condensation or evaporation and thus serves well as a tracer of the movement of air parcels in the atmosphere. The temperature-dependent form of the water-vapor mixing ratio equation is now derived.

B. Calculation of the Water-Vapor Mixing Ratio from the Lidar Equation

From Eq. (2), the ratio of the single-scattering Raman lidar measurements of water vapor and nitrogen, in-

cluding the effects of temperature sensitivity, can be represented as

$$\frac{P(\Delta\lambda_H, r)}{P(\Delta\lambda_N, r)} = \frac{O_H(r) F_H[T(r)] N_H(r) [d\sigma_H(\pi)/d\Omega] \xi(\lambda_H)}{O_N(r) F_N[T(r)] N_N(r) [d\sigma_N(\pi)/d\Omega] \xi(\lambda_N)} \times \Delta\tau(\lambda_H, \lambda_N, r), \quad (4)$$

where the shorthand notation

$$\Delta\tau(\lambda_H, \lambda_N, r) = \exp\left\{-\int_0^r [\alpha(\lambda_H, r') - \alpha(\lambda_N, r')] dr'\right\} \quad (5)$$

has been used for the differential transmission term, which accounts for the fact that atmospheric transmission differs at the two Raman wavelengths. Note the useful property that $\Delta\tau(\lambda_H, \lambda_N, r) = 1/\Delta\tau(\lambda_N, \lambda_H, r)$. We recall that the water-vapor mixing ratio is the ratio of the mass of water vapor to the mass of dry air and consider that N_2 forms a constant fraction (~ 0.78) of dry air in the lower atmosphere; it is apparent that

$$w = \frac{MW_{H_2O}}{MW_{DryAir}} \frac{N_H(r)}{N_{DryAir}(r)} \cong \frac{MW_{H_2O}}{MW_{DryAir}} \frac{N_H(r)}{N_N(r)/0.78} \cong 0.485 \frac{N_H(r)}{N_N(r)}, \quad (6)$$

where w is the water-vapor mixing ratio, MW_{H_2O} is the molecular weight of water vapor (~ 18 g/mol), and MW_{Air} is the molecular weight of dry air [an averaged quantity whose value is ~ 28.94 g/mol (Ref. 7)]. Combining Eqs. (4) and (6) yields

$$w = k \frac{O_N(r) F_N(T) P(\lambda_H, r) [d\sigma_N(\pi)/d\Omega] \xi(\lambda_N)}{O_H(r) F_H(T) P(\lambda_N, r) [d\sigma_H(\pi)/d\Omega] \xi(\lambda_H)} \times \Delta\tau(\lambda_N, \lambda_H, r), \quad (7)$$

where the constant of proportionality from Eq. 6 is represented as k ($\cong 0.485$).

For a perfect optical system the ratio $O_N(r)/O_L(r)$ would be unity throughout the range of measurement. In a real lidar system this ratio typically departs from unity for the ranges closest to the telescope. If this departure from unity is significant for the quantity being determined, one can quantify the ratio of the overlap functions by taking data in both channels, using a common N_2 or O_2 interference filter,^{8,9} or by using more-analytical techniques.¹⁰ In the application of the common filter approach for quantifying the overlap function, care must be taken to use filters that are all of similar width because narrower filters are more subject to changes in transmission owing to the different divergence angles that arise in the near field.¹¹ In other words, the common molecular filter should possess transmission characteristics that are similar to those of the filters used for normal data acquisition. Furthermore, it is important to study the transmission and polarization characteristics of any intervening optics to ensure that

these properties do not change significantly between the nitrogen (or oxygen) wavelength used for determination of the overlap function and the wavelength of the species being measured in a given channel.

Another technique that can be used to reduce the influence of the overlap function is to acquire data at a small angle above the horizon, assume horizontal homogeneity over the atmosphere within a few kilometers of the lidar location, and convert the angle data to vertical data. This procedure can limit the influence of the lidar overlap functions on the calculation of the water-vapor mixing ratio to approximately the lowest 10–50 m of the atmosphere.¹² Above this point, $O_N(r)/O_H(r)$ may then be considered constant and equal to unity. For either of these approaches, above some point in the vertical profile, which can be as little as 10–50 m above the lidar site, the overlap functions no longer have an influence.

The water-vapor mixing ratio equation can now be expressed by use of a single calibration factor as follows:

$$w = k^*(r) \frac{F_N[T(r)] P(\lambda_H, r)}{F_H[T(r)] P(\lambda_N, r)} \Delta\tau(\lambda_N, \lambda_H, r), \quad (8)$$

$$k^*(r) \cong 0.485 \frac{O_N(r) [d\sigma_N(\pi)/d\Omega] \xi(\lambda_N)}{O_H(r) [d\sigma_H(\pi)/d\Omega] \xi(\lambda_H)}, \quad (9)$$

where $k^*(r)$ is now the lidar system's calibration factor. The temperature-dependent ratio $F_N[T(r)]/F_H[T(r)]$, which is addressed in Subsection 3.C, now appears as a multiplier of the traditional Raman lidar water-vapor mixing ratio equation.^{9,13,14}

The appropriate cross section values for different laser output wavelengths can be determined by use of known values of cross section at 337.1 nm ($\text{cm}^2 \text{sr}^{-1}$) (Ref. 15) and by accounting for the $(\nu - \Delta\nu)^4$ scaling of molecular scattering, where $\Delta\nu$ is the Raman frequency shift if such is present. Following this procedure for the XeF excimer laser (351.1 nm), the tripled Nd:YAG laser (354.7 nm), and the double Nd:YAG laser (532.1 nm) yields the following expressions for $k^*(r)$:

$$k_{351}^*(r) \cong 0.485 \frac{O_N(r) 2.9 \times 10^{-30} \xi(\lambda_N)}{O_H(r) 6.5 \times 10^{-30} \xi(\lambda_H)} \cong 0.22 \frac{O_N(r) \xi(\lambda_N)}{O_H(r) \xi(\lambda_H)}, \quad (10)$$

$$k_{355}^*(r) \cong 0.485 \frac{O_N(r) 2.8 \times 10^{-30} \xi(\lambda_N)}{O_H(r) 6.2 \times 10^{-30} \xi(\lambda_H)} \cong 0.22 \frac{O_N(r) \xi(\lambda_N)}{O_H(r) \xi(\lambda_H)}, \quad (11)$$

$$k_{532}^*(r) \cong 0.485 \frac{O_N(r) 4.6 \times 10^{-31} \xi(\lambda_N)}{O_H(r) 8.9 \times 10^{-31} \xi(\lambda_H)} \cong 0.25 \frac{O_N(r) \xi(\lambda_N)}{O_H(r) \xi(\lambda_H)}. \quad (12)$$

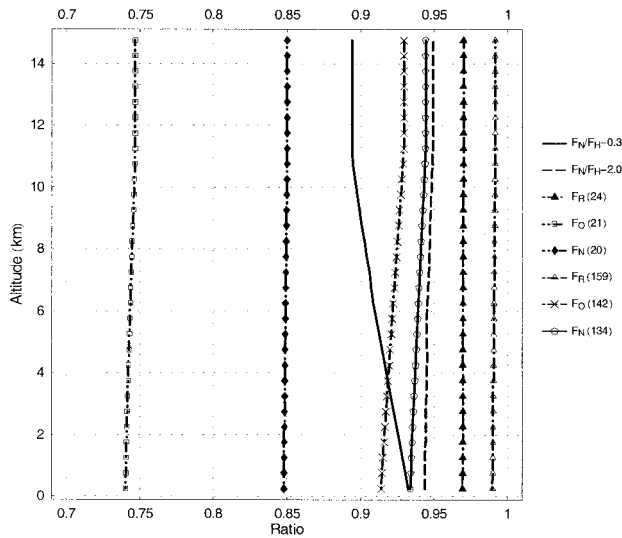


Fig. 1. Temperature-dependent ratios $F_N[T(r)]/F_H[T(r)]$ needed for evaluating the water-vapor mixing ratio plotted with passbands for the water-vapor and N_2 channels that correspond to 0.3 and 2.0 nm when they are excited by 354.7-nm radiation. For the choice of 0.3-nm passband for both water vapor and nitrogen the temperature-dependent ratio decreases by $\sim 4\%$ between the surface and 11 km. Narrower water-vapor passbands increase the magnitude of this change. The temperature-dependent functions F_R , F_N , and F_O that are needed for calculation of the aerosol scattering ratio are also shown for the same passband conditions. For example, a 24-cm^{-1} passband for the Rayleigh–Mie signal corresponds to 0.3 nm when 354.7-nm excitation is used.

Expressions (10)–(12) for the k^* factors demonstrate that the ratio of Raman cross sections is not constant as a function of exciting wavelength because $\Delta\nu$ is different for Raman scattering from N_2 and H_2O .

C. Temperature-Sensitivity Functions versus Altitude

The temperature-sensitivity ratio $F_N[T(r)]/F_H[T(r)]$ that is needed for evaluating Eq. (8) is plotted in Fig. 1 versus altitude, assuming a U.S. Standard Atmosphere temperature profile.¹⁶ The following passbands were used for this illustration: water vapor, 18 and 120 cm^{-1} ; N_2 , 20 and 134 cm^{-1} , which correspond to ~ 0.3 - and 2.0 -nm passbands for 354.7-nm excitation, as indicated in the figure. The 0.3-nm passband approximates that of such systems as the U.S. Department of Energy's Raman lidar¹⁷ and the NASA/Goddard Space Flight Center's Scanning Raman Lidar (SRL) in its daytime measurement configuration.¹⁸ The other temperature-sensitivity functions, $F_R(r)$, $F_O(r)$, and $F_N(r)$, are needed for calculation of the aerosol scattering ratio, which is treated below. They are also displayed with passband widths that correspond to 0.3 and 2.0 nm when 354.7-nm excitation is used.

It is interesting to note that, for $F_N[T(r)]/F_H[T(r)]$ pertinent to the calculation of water-vapor mixing ratio, the use of a narrow passband (0.3 nm for 354.7-nm excitation) for both water-vapor and nitrogen channels yields a temperature sensitivity ratio that decreases approximately 4% between the sur-

face and 11 km, whereas the use of a wide passband (2.0 nm) for both channels yields a ratio that increases approximately 0.6% over the same range. Other combinations of passband widths and positions can increase this effect to much larger than 5%.¹ It is apparent from this analysis that certain combinations of passband center and width for the two channels can be found that yield an altitude-independent ratio. For example, the combination of approximately 55-cm^{-1} passbands for both water vapor and N_2 would yield a ratio of $F_N[T(r)]/F_H[T(r)]$ that is independent of height.¹ The error equations for the mixing ratio are now formulated.

D. Equations for Water-Vapor Mixing Ratio Error

The random error in determining w is found by application of standard error propagation formulas¹⁹ to Eq. (8). The result, which has been presented before²⁰ but is repeated here for completeness, is

$$\frac{\sigma_w^2}{w^2} = \frac{\sigma_{k^*}^2}{k^{*2}} + \frac{\sigma_{R_w}^2}{R_w^2} + \frac{\sigma_{\Delta\tau}^2}{\Delta\tau^2}, \quad (13)$$

where the abbreviation $R_w = P(\lambda_H, r)/P(\lambda_N, r)$ has been used. The full quantification of Eq. (13) requires analysis of the variation of all random factors that go into the calibration of the water-vapor mixing ratio. The Raman lidar calibration has been shown to be highly stable over periods of years^{14,21} when system components are not changed; thus the variance in k^* can be considered to be small. Errors introduced by uncertainties in the water-vapor mixing ratio differential transmission term are studied in Subsection 3.E, where it is shown that, by using the Raman lidar measurement of aerosol extinction in addition to molecular number density obtained from radiosonde, one can keep the error in this term very small also. Thus the random error in the ratio of the lidar signals usually dominates the error budget. These errors are now quantified by use of Poisson statistics.

Recalling that the P terms in Eq. (8) are actually background-subtracted quantities, one may reexpress $\sigma_{R_w}^2/R_w^2$ by using the following substitutions: $P(\lambda_H, r) = S_H - B_H$ and $P(\lambda_N, r) = S_N - B_N$, where S refers to the laser-induced signals and B refers to the background terms, as follows:

$$\frac{\sigma_{R_w}^2}{R_w^2} = \frac{\sigma_{SH}^2 + \sigma_{BH}^2}{(S_H - B_H)^2} + \frac{\sigma_{SN}^2 + \sigma_{BN}^2}{(S_N - B_N)^2}, \quad (14)$$

$$\sigma_{R_w}^2 = \frac{(S_H - B_H)^2}{(S_N - B_N)^2} \left[\frac{\sigma_{SH}^2 + \sigma_{BH}^2}{(S_H - B_H)^2} + \frac{\sigma_{SN}^2 + \sigma_{BN}^2}{(S_N - B_N)^2} \right], \quad (15)$$

where it is explicitly shown that there is error in the determination of the backgrounds. Under certain conditions, such as high background during daytime measurements, these error sources can become significant.

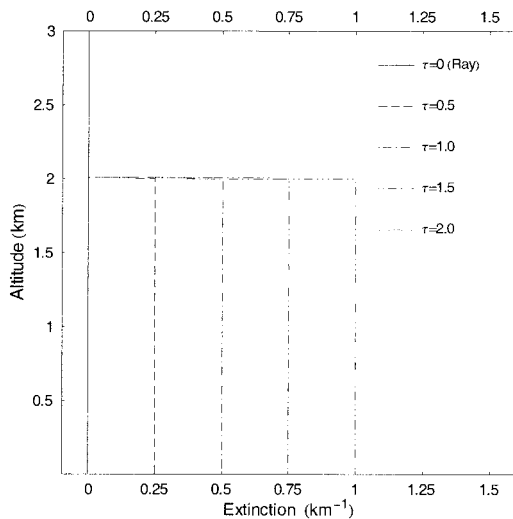


Fig. 2. Five synthesized aerosol extinction profiles to test the influence of various aerosol loadings on the calculation of DT. The aerosol optical depth of the profiles ranges from $\tau = 0$ (pure Rayleigh) to $\tau = 2.0$ (extremely hazy). All profiles equal 0 above 2.0 km.

E. Water-Vapor Mixing Ratio Differential Transmission

The differential transmission (DT) term $\Delta\tau(\lambda_N, \lambda_H, r)$ in Eq. (28) below, which accounts for the fact that the return signals at λ_N and λ_H experience different amounts of attenuation on their return trips from the scattering volume, are now computed. The influence of various aerosol loadings on this calculation are studied by use of several synthesized aerosol extinction profiles.

The synthesized profiles are shown in Fig. 2, where each of the profiles equals zero above an altitude of 2

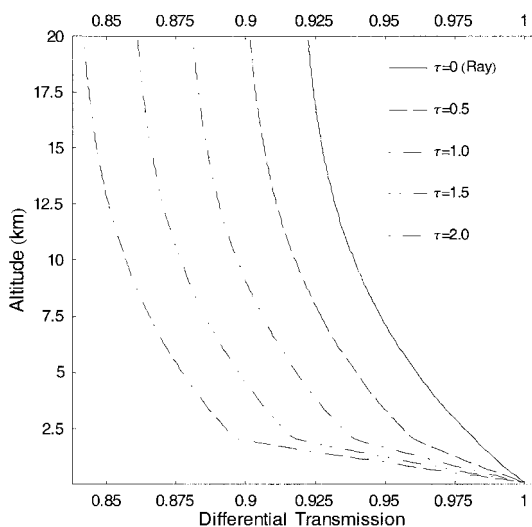


Fig. 3. Differential transmission term for calculation of the water-vapor mixing ratio when the XeF excimer laser (351.1 nm) or the Nd:YAG laser (354.7 nm) is used. Various modeled aerosol loadings ranging from a pure Rayleigh atmosphere to extremely hazy ($\tau = 2.0$) are considered. Changes in aerosol optical depth of 0.5 change the DT by approximately 2%.

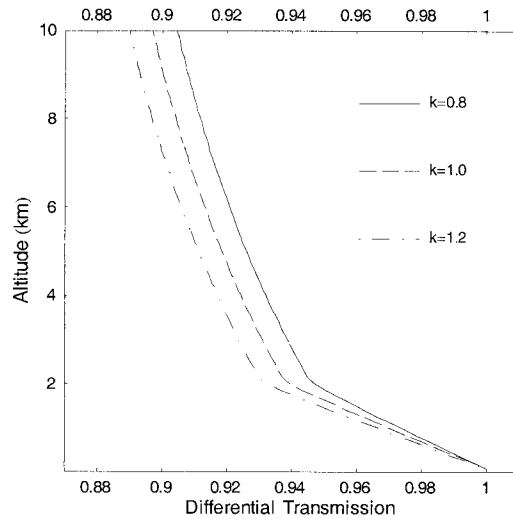


Fig. 4. DT profile for calculation of the water-vapor mixing ratio for an aerosol optical depth of 1.0; the Angstrom coefficient is allowed to vary from 0.8 to 1.2. The DT term changes by less than 2% over this range of k . The profiles are appropriate for a laser output wavelength of 351–355 nm.

km. These aerosol extinction profiles, along with the molecular extinction calculated by the techniques outlined in part 1¹ with the molecular number density values from the U.S. Standard Atmosphere,¹⁶ were used for calculating the water-vapor DT profiles shown in Fig. 3. The profiles can be considered appropriate for water-vapor mixing ratio measurements made with either the XeF excimer (351.1 nm) or the tripled Nd:YAG (355 nm) laser because the DT values differ by less than 1% for these two cases. The aerosol optical depth, considered to be at the laser wavelength, for each of these profiles is obtained by integration of the extinction from 0 to 2 km. The aerosol optical depths τ that result are shown in the figure. They range from a pure Rayleigh atmosphere ($\tau = 0$) to the extremely hazy value $\tau = 2.0$. In these plots, a range independent Angstrom coefficient of $k = 1.0$ was used.

For a pure Rayleigh atmosphere the value of the water vapor's DT varies from 1 at the surface to approximately 0.92 at 20 km. For an aerosol optical depth of 0.5 the range of values increases to 1.0–0.90. As aerosol loading increases, the DT values become smaller. Notice that the curves are all parallel above 2 km. This comparison shows the importance, particularly under hazy conditions, of having a simultaneous measurement of aerosol extinction for the calculation of differential transmission.

Because the Raman lidar can be used to measure the round-trip aerosol extinction directly, actual lidar profiles of aerosol extinction can be used to generate the required DT term. However, there still remains the uncertainty in what value of $k(r)$ to use in the calculation of the one-way aerosol extinction because variations in k influence the Raman-derived extinction.^{1,12} Additional aerosol information such as provided by a sunphotometer, although it is limited to

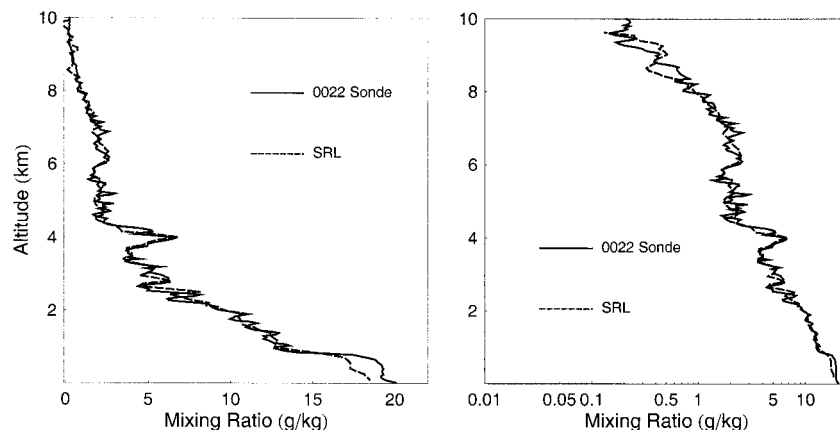


Fig. 5. Comparison of a 10-min SRL water-vapor mixing ratio profile with radiosonde shown with a linear scale at the left and a log scale at the right. The SRL water-vapor calibration was determined through a best-fit procedure between the lidar and the radiosonde at 1–3 km. The radiosonde was launched at 0022 UT.

total column averages, can be useful in this analysis. To test the sensitivity of the differential transmission to changes in Angstrom coefficient k for an upward-looking system with an output wavelength of 351–355 nm, Fig. 4 was generated by use of various values of k for an aerosol optical depth of 1.0. Varying k from 0.8 to 1.2 causes less than a 2% change in the DT. The relatively low sensitivity of the differential transmission to variations in k implies that variations in $k(r)$ within the column will have a small influence on the profile of DT under most circumstances.

The doubled Nd:YAG laser (~ 532 nm) is a less popular choice for making water-vapor mixing ratio measurements than UV lasers such as the tripled Nd:YAG (~ 355 nm) for several reasons, including the reduced Raman scattering cross section, lower efficiency of detectors for use at the water-vapor shifted wavelength of ~ 660 nm, and the fact that water vapor absorbs weakly at 660 nm but not at 607 nm. This difference in absorption between 607 and 660 nm implies that the calculation of the DT that is needed in Eq. (8) must account for both scattering and absorption. A radiative transfer model such as Modtran²² can be used for this calculation. With the doubled Nd:YAG exciting wavelength (~ 532 nm), the DT at 20 km due only to molecular and aerosol scattering will change from ~ 0.98 for a pure Rayleigh atmosphere to ~ 0.92 , assuming an aerosol thickness of $\tau = 1.0$. However, absorption due to water vapor will decrease these values of DT at 20 km by as much as 1%, as determined by Modtran calculations that use the standard tropical atmosphere. To obtain the DT profile with the highest accuracy would require an iteration because in the Raman lidar equation, water vapor is responsible for both backscatter and extinction.

F. Calibration of Raman Lidar Water-Vapor Mixing Ratio

The issue of lidar calibration is important because calibration is the process that leads to useful meteorological quantities. Various approaches have been

taken in the effort to calibrate the water-vapor measurements of a Raman lidar system. Among them are (1) an atmospheric calibration, assuming saturation at cloud base,²³ (2) comparison with another water-vapor sensor such as a radiosonde²¹ or a microwave radiometer,¹⁴ and (3) a first-principles calibration that accounts for the total efficiency of transmitting photons through the atmosphere, scattering them off the molecules of interest and then detecting them with the lidar receiver system.^{8,24}

1. Calibration with Respect to Other Water-Vapor Sensors and at the Base of Clouds

The NASA/Goddard Space Flight Center Scanning Raman Lidar (SRL) was stationed on Andros Island, Bahamas, during July–September 1998 for the third convection and moisture (CAMEX-3) hurricane study program.²³ At the time of that deployment, the SRL used a XeF excimer laser (351 nm), a 0.76-m telescope, and high- and low-range photomultiplier tubes to measure each of the Rayleigh–Mie, oxygen, nitrogen, and water-vapor signals.¹⁸ The passbands of the water-vapor and nitrogen channels were 8.6 and 8.0 nm, respectively. It is important to note that use of such wide spectral passbands essentially eliminates the issues relating to temperature sensitivity studied here.²⁵

The final SRL water-vapor mixing ratio calibration constant for the CAMEX-3 campaign was derived in two ways that resulted in nearly identical values. One was through the use of 31 Vaisala RS-80 radiosonde comparisons, in which the radiosondes were corrected for the known dry bias in the sondes.^{26,27} The other technique was based on a set of lidar water-vapor and radiosonde temperature measurements made at the base of marine boundary layer cumulus clouds, assuming that saturation obtained at cloud base.²³ The mean calibration constant derived by these two techniques differed by less than 1%, indicating that, at least for the CAMEX-3 campaign, the Vaisala dry bias correction performed well. The standard deviation of the cloud-base-derived calibra-

tion constant was 3%, whereas that of the radiosonde-derived calibration constant was 5%, indicating that the cloud base technique was a more stable calibration source than the radiosonde.

An example of a lidar–radiosonde comparison is shown in Fig. 5 for data acquired over a 10-min period on 22 August 1998 at Andros Island during the CAMEX-3 program. The lidar calibration constant, k^* , from relation (10) and determined by the cloud base calibration technique was ~ 0.204 . Using this value of k^* in Eq. (8) produces the lidar water vapor mixing ratio in units of kilograms of water vapor per kilogram of dry air. The units of mixing ratio typically used in these plots, however, are grams of water vapor per kilogram of dry air (g/kg), which we obtain by multiplying k^* by 1000. It is interesting to note that the calibration value of 0.204 indicates that, from relation (10), the ratio of lidar system efficiencies is $\xi(\lambda_N)/\xi(\lambda_H) = 0.204/0.22 \cong 0.93$. In other words, at the time of the CAMEX-3 deployment the SRL optical detection system had $\sim 7\%$ higher efficiency in the water-vapor channel than in the N_2 channel. This is the result of an optical design that maximized the transmission of the water-vapor wavelength at the expense of the other (stronger) signals such as N_2 .

The data are shown in the figure both on a linear scale at the left and on a log scale at the right. The linear scale shows the discrepancy between the lidar and the radiosonde in the first kilometer, with the radiosonde showing a low-level moisture inversion. This may be a real event in the atmosphere, or it could be an indication that the radiosonde has required some time to equilibrate to the environment,²⁸ or it could be an unresolved overlap issue in the lidar system. The log scale at the right in Fig. 5 shows the good agreement of the two sensors in the upper regions of the profile where mixing ratio values approach 0.1 g/kg. The lidar data at the left are plotted with 75-m vertical resolution. The lidar data at the right use 75-m resolution below 6 km, 225 m resolution from 6 to 8 km, and 375 m above 8 km. In general the random error increases with height and reaches approximately 20% at 10 km.

Another method of calibration is that used by the U.S. Department of Energy's Cloud and Radiation Testbed (CART) Raman lidar (CARL), which is calibrated by comparison of the total precipitable water of the lidar profile and that of a collocated microwave radiometer.¹⁴ The calibration constant derived from this technique has proved to be stable. Between August 1998 and January 2000 the standard deviation of the CARL calibration constant was 3%, whereas the standard error of this constant was 0.04%,²⁹ thus demonstrating that, if no changes are made to a Raman water-vapor lidar system, stable long-term calibration is possible.

2. First-Principles Raman Water-Vapor Lidar Calibration

Examination of relation (8) indicates that a first-principles Raman water-vapor lidar calibration requires knowledge of the ratio of transmissions of the

lidar water-vapor and N_2 channels, the ratio of Raman scattering cross sections from N_2 (or O_2) and water vapor, the temperature-dependent functions, and the DT. So far in this paper we have discussed ways in which to determine the two last-named quantities with accuracies of approximately 1–2%. To pursue an absolute calibration we must quantify the ratio of lidar channel transmissions and the ratio of Raman cross sections with accuracy as well.

The efficiency ratio $\xi(\lambda_N)/\xi(\lambda_H)$ can be determined with high accuracy through the use of a blackbody calibration lamp. For example, UV calibration lamps that are traceable to the National Institutes of Standards and Technology with 2% accuracy are easily available. The 2% uncertainty in the intensity of the lamp source is due to the uncertainty in the effective color temperature of the lamp, which for a 2% error in intensity is ~ 5 K. However, it is the ratio of intensities at λ_N and λ_H that is needed for the Raman lidar calibration, and a lamp with 2% absolute accuracy can be used to quantify the ratio of intensities at two closely spaced wavelengths such as λ_N and λ_H to within $\sim 0.1\%$. Therefore a highly accurate calibration source is available for quantifying $\xi(\lambda_N)/\xi(\lambda_H)$.

Knowledge of the ratio of cross sections $[d\sigma_N(\pi)/d\Omega]/[d\sigma_H(\pi)/d\Omega]$ is limited by the fact that the best available laboratory measurements of the water-vapor cross section date from 1976 and have an uncertainty of $\pm 10\%$.³⁰ Therefore any absolute calibration effort that relies on the currently available Raman cross sections for N_2 and water vapor will have a total error that exceeds 10%. The first documented effort to perform an absolute Raman water-vapor calibration was made by Vaughan *et al.*⁸ Their effort resulted in an error estimate of 12%, whereas the more recent effort of Sherlock *et al.*²⁴ estimated a total error of 12–14%. The largest uncertainty in both of these efforts was in the knowledge of the Raman cross-section ratio for N_2 and water vapor.

The relative line strengths in the Raman spectra from water vapor,³¹ N_2 and O_2 ^{32–34} can now be modeled with high precision. This ability, coupled with an accurate measurement of $\xi(\lambda_N)/\xi(\lambda_H)$ for the lidar system and an accurate calibration with respect to another sensor, could potentially be used to improve the knowledge of the ratio of N_2 and water-vapor cross sections. For example, the standard error of the CARL calibration constant with respect to the U.S. Department of Energy's Atmospheric Radiation Measurement (ARM) microwave radiometer, which is believed to possess an absolute water-vapor accuracy of better than 4% for precipitable water amounts in excess of 1 cm,³⁵ is 0.04%. In other words, the CART Raman lidar calibration is highly stable and well determined. That, coupled with the high relative accuracy in the line strengths of the Raman water-vapor and N_2 spectra available through modeling, implies that stable, long-term measurements of the lidar calibration constant such as those of the CART Raman lidar, coupled with radiometric measurements of the optical transmission efficiency,

could be used to improve the knowledge of the atmospheric cross-section ratio $[d\sigma_N(\pi)/d\Omega]/[d\sigma_H(\pi)/d\Omega]$. Measurement of the cross-section ratio with an accuracy of 4–5% appears possible. Therefore it seems feasible that an absolute Raman water-vapor lidar calibration could be performed in the future with total error of perhaps 5–7% by use of this approach.

4. Aerosol Scattering Ratio

A. Definitions

The aerosol scattering ratio is used to quantify the ratio of aerosol (or Mie scattering) to molecular scattering. It is defined as the ratio of the volume backscatter coefficients for total (molecular plus aerosol) scattering to pure molecular scattering and can be expressed as

$$\begin{aligned}\mathcal{R}(\lambda_L, r) &= \frac{\beta_{\pi}^{\text{tot}}(\lambda_L, r)}{\beta_{\pi}^{\text{mol}}(\lambda_L, r)} = \frac{\beta_{\pi}^{\text{mol}}(\lambda_L, r) + \beta_{\pi}^{\text{aer}}(\lambda_L, r)}{\beta_{\pi}^{\text{mol}}(\lambda_L, r)} \\ &= 1 + \frac{\beta_{\pi}^{\text{aer}}(\lambda_L, r)}{\beta_{\pi}^{\text{mol}}(\lambda_L, r)},\end{aligned}\quad (16)$$

where the volume backscatter coefficient for molecules $\beta_{\pi}^{\text{mol}}(\lambda_L, r)$ is given by $N^{\text{mol}}(r)d\sigma_{\text{mol}}(\pi)/d\Omega$.¹

B. Formulation of the Equations for Aerosol Scattering Ratio

The Raman lidar is able to quantify the aerosol scattering ratio in a more direct manner than are Rayleigh–Mie lidar systems. The Raman lidar measures a signal that is proportional to the molecular nitrogen (or oxygen) density. This signal can be used as a direct quantification of the denominator needed in Eq. (16). A simple Rayleigh–Mie lidar has no such signal and must resort to inversions to determine this ratio.

The calculation of the aerosol scattering ratio from the basic Raman lidar signals is now described. Forming the ratio of Eqs. (1) and (2) for the background-subtracted lidar-received power at laser wavelength λ_L and at Raman N_2 wavelength λ_N yields

$$\frac{P(\Delta\lambda_R, r)}{P(\Delta\lambda_N, r)} = \frac{O_R(r)}{O_N(r)} \frac{\xi(\lambda_L)}{\xi(\lambda_N)} \frac{F_R[T(r)]}{F_N[T(r)]} \frac{\beta_{\pi}^{\text{mol}}(\lambda_L, r) + \beta_{\pi}^{\text{aer}}(\lambda_L, r)}{N_N(r)[d\sigma_N(\pi)/d\Omega]} \exp\left\{-\int_0^r [\alpha(\lambda_L, r') - \alpha(\lambda_N, r')]dr'\right\} \quad (17)$$

$$= \frac{O_R(r)}{O_N(r)} \frac{\xi(\lambda_L)}{\xi(\lambda_N)} \frac{F_R[T(r)]}{F_N[T(r)]} \frac{\beta_{\pi}^{\text{mol}}(\lambda_L, r) + \beta_{\pi}^{\text{aer}}(\lambda_L, r)}{N_N(r)[d\sigma_N(\pi)/d\Omega]} \Delta\tau(\lambda_L, \lambda_N, r). \quad (18)$$

The Raman backscatter coefficient for N_2 molecules is $\beta_{\pi}^N(\lambda_L, r) = N_N(r)d\sigma_N(\pi)/d\Omega$ and is proportional to the Rayleigh backscattering coefficient for air because N_2 is well mixed in the lower atmosphere. This fact can be expressed as

$$\beta_{\pi}^N(\lambda_L, r) = C_N \beta_{\pi}^{\text{mol}}(\lambda_L, r). \quad (19)$$

If the Raman O_2 signal is used to normalize the scattering ratio, then the following equation pertains:

$$\beta_{\pi}^O(\lambda_L, r) = C_O \beta_{\pi}^{\text{mol}}(\lambda_L, r). \quad (20)$$

The proportionality factor C_N in Eq. (19) can be calculated for the use of different laser sources by scaling of cross-section values from 337.1 nm (Ref. 15) and from the fact that N_2 and O_2 form ~ 0.78 and ~ 0.21 of the atmosphere, respectively, as follows:

$$\begin{aligned}C_N(\lambda_L = 351) &\cong \frac{1}{0.78} \frac{\beta_{\pi}^N(\lambda_L = 351, r)}{\beta_{\pi}^{\text{mol}}(\lambda_L = 351, r)} \\ &\cong \frac{1}{0.78} \frac{2.9 \times 10^{-30}}{3.3 \times 10^{-27}} \cong 1.1 \times 10^{-3},\end{aligned}\quad (21)$$

$$\begin{aligned}C_N(\lambda_L = 355) &\cong \frac{1}{0.78} \frac{\beta_{\pi}^N(\lambda_L = 355, r)}{\beta_{\pi}^{\text{mol}}(\lambda_L = 355, r)} \\ &\cong \frac{1}{0.78} \frac{2.8 \times 10^{-30}}{3.2 \times 10^{-27}} \cong 1.1 \times 10^{-3},\end{aligned}\quad (22)$$

$$\begin{aligned}C_N(\lambda_L = 532) &\cong \frac{1}{0.78} \frac{\beta_{\pi}^N(\lambda_L = 532, r)}{\beta_{\pi}^{\text{mol}}(\lambda_L = 532, r)} \\ &\cong \frac{1}{0.78} \frac{4.6 \times 10^{-31}}{6.3 \times 10^{-28}} \cong 9.4 \times 10^{-4}.\end{aligned}\quad (23)$$

The appropriate constants for use of the Raman O_2 in normalizing the scattering ratio are

$$\begin{aligned}C_O(\lambda_L = 351) &\cong \frac{1}{0.21} \frac{\beta_{\pi}^O(\lambda_L = 351, r)}{\beta_{\pi}^{\text{mol}}(\lambda_L = 351, r)} \\ &\cong \frac{1}{0.21} \frac{3.9 \times 10^{-30}}{3.3 \times 10^{-27}} \cong 5.6 \times 10^{-3},\end{aligned}\quad (24)$$

$$\begin{aligned}C_O(\lambda_L = 355) &\cong \frac{1}{0.21} \frac{\beta_{\pi}^O(\lambda_L = 355, r)}{\beta_{\pi}^{\text{mol}}(\lambda_L = 355, r)} \\ &\cong \frac{1}{0.21} \frac{3.7 \times 10^{-30}}{3.2 \times 10^{-27}} \cong 5.6 \times 10^{-3},\end{aligned}\quad (25)$$

$$\begin{aligned}C_O(\lambda_L = 532) &\cong \frac{1}{0.21} \frac{\beta_{\pi}^O(\lambda_L = 532, r)}{\beta_{\pi}^{\text{mol}}(\lambda_L = 532, r)} \\ &\cong \frac{1}{0.21} \frac{6.5 \times 10^{-31}}{6.3 \times 10^{-28}} \cong 4.9 \times 10^{-3}.\end{aligned}\quad (26)$$

Equations (18) and (19) can now be combined to

yield an expression for $\mathcal{R}(\lambda_L, r)$. The result is

$$\begin{aligned} \mathcal{R}(\lambda_L, r) - 1 &= \frac{\beta_{\pi}^{\text{aer}}(\lambda_L, r)}{\beta_{\pi}^{\text{mol}}(\lambda_L, r)} = C_N(\lambda_L) F_N[T(r)] \\ &\times \frac{O_N(r)}{O_R(r)} \frac{\xi(\lambda_N)}{\xi(\lambda_L)} \frac{P(\Delta\lambda_R, r)}{P(\Delta\lambda_N, r)} \Delta\tau(\lambda_N, \lambda_L, r) \\ &- F_R[T(r)]. \end{aligned} \quad (27)$$

A similar expression can be derived for the use of Raman O_2 as the normalizing signal in the scatter-ingratio. Absorbing the overlap and efficiencies from Eq. (27) into a new term, $C_N^*(\lambda_L, r)$, yields

$$\begin{aligned} \mathcal{R}(\lambda_L, r) - 1 &= C_N^*(\lambda_L, r) F_N[T(r)] \frac{P(\Delta\lambda_L, r)}{P(\Delta\lambda_N, r)} \\ &\times \Delta\tau(\lambda_N, \lambda_L, r) - F_R[T(r)], \end{aligned} \quad (28)$$

$$C_N^*(\lambda_L, r) = C_N(\lambda_L) \frac{O_N(r)}{O_R(r)} \frac{\xi(\lambda_N)}{\xi(\lambda_L)}. \quad (29)$$

Because in Eq. (18) $F_R[T(r)]$ multiplies only $\beta_{\pi}^{\text{mol}}(\lambda_L, r)$ and not $\beta_{\pi}^{\text{aer}}(\lambda_L, r)$, the result achieved in Eq. (28) for the aerosol scattering ratio is not simply a temperature-dependent factor times the traditional result,^{9,12–14} as it was for the water-vapor mixing ratio. The effect of the temperature-dependent functions in Eq. (28) is discussed in Subsection 4.F.1 below, which concerns atmospheric calibration of the aerosol scattering ratio.

C. Temperature-Sensitivity Factors for the Scattering Ratio Calculation

The temperature-sensitivity functions $F_R(r)$, $F_O(r)$, and $F_N(r)$ needed for evaluating Eq. (28) were shown in Fig. 1. $F_O(r)$ was included in the figure because the Raman signal from molecular oxygen can be used equally well in forming the aerosol scattering ratio. There is an advantage in doing so when it comes to calculating the differential transmission function, as will be shown presently. In general, $F_X(r)[d\sigma_X(\pi)/d\Omega]$ quantifies the effective molecular cross section consistent with the use of a monochromatic optical efficiency term $\xi(\lambda_X)$ in the lidar equation. A narrower passband transmits less of the rotational (or vibrational–rotational) Raman lines and thus less of the total cross section. In the case of O_2 , the fraction of total cross section that is present in the vibrational–rotational lines is larger than for N_2 , as shown in Fig. 1. Thus, for comparable temperatures and passband widths, $F_O(r)$ has a smaller value than $F_N(r)$. The evaluation of the calibration constant $C_{N,O}^*(\lambda_L, r)$ and the DT term is discussed after the error equations are developed.

D. Equations for Aerosol Scattering Ratio Error

The random component of the error in determining $\mathcal{R}(\lambda_L, r)$ is given by application of standard error propagation formulas¹⁹ to Eq. (28). The result is

$$\frac{\sigma_{\mathcal{R}}^2}{\mathcal{R}^2} = \frac{\sigma_{C_N^*}^2}{C_N^{*2}} + \frac{\sigma_A^2}{A^2} + \frac{\sigma_{\Delta\tau}^2}{\Delta\tau^2}, \quad (30)$$

$$\sigma_{\mathcal{R}}^2 = T^2 \left(\frac{\sigma_{C_N^*}^2}{C_N^{*2}} + \frac{\sigma_{F_N}^2}{F_N^2} + \frac{\sigma_A^2}{A^2} + \frac{\sigma_{\Delta\tau}^2}{\Delta\tau^2} \right) + \sigma_{F_R}^2, \quad (31)$$

where the following shorthand notation has been used:

$$T = C_N^*(\lambda_L, r) F_N[T(r)] A \Delta\tau(\lambda_N, \lambda_L, r), \quad (32)$$

$$A = \frac{P(\Delta\lambda_R, r)}{P(\Delta\lambda_N, r)}, \quad (33)$$

where A represents the ratio of the background-subtracted lidar signals, $P(\Delta\lambda_R, r)/P(\Delta\lambda_N, r)$, in Eq. (28). Variations in the calibration factor, $C_N^*(\lambda_L, r)$, and in the differential transmission, $\Delta\tau$, are studied below. It is shown that the atmosphere offers a natural calibration tool that permits accurate scattering ratio calibrations. Furthermore, errors in the DT term can be kept small through a direct measurement of aerosol extinction. Quantifying the error in the knowledge of the temperature-sensitivity functions $F_N(T)$ [or $F_O(T)$] and $F_R(T)$ is rather complex because the error is related to the uncertainty in the passband shape, the atmospheric temperature, and the spectrum of the molecular feature that is being measured. However, the overall effect of both of these temperature-dependent functions on calculation of the scattering ratio is of the order of 10%. The uncertainty in the calculation of the temperature-dependent functions can be made less than 10%, implying that the contribution of the temperature dependence to the error budget can be kept below 1%. Therefore the random error in calculation of the scattering ratio is typically dominated by the uncertainty in the lidar signals themselves. Therefore, quantifying the standard error in the aerosol scattering ratio as being determined by the random error in the lidar signals is a good approximation. The equations are

$$\frac{\sigma_{\mathcal{R}}^2}{\mathcal{R}^2} \equiv \frac{\sigma_{SL}^2 + \sigma_{BL}^2}{(S_L - B_L)^2} + \frac{\sigma_{SN}^2 + \sigma_{BN}^2}{(S_N - B_N)^2}, \quad (34)$$

$$\sigma_{\mathcal{R}}^2 \equiv \frac{(S_L - B_L)^2}{(S_N - B_N)^2} \left[\frac{\sigma_{SL}^2 + \sigma_{BL}^2}{(S_L - B_L)^2} + \frac{\sigma_{SN}^2 + \sigma_{BN}^2}{(S_N - B_N)^2} \right], \quad (35)$$

where the subscripts L and N refer to the signals at the laser wavelength and at the Raman-shifted N_2 wavelength, respectively. A point to note here is that the errors in the determination of the backgrounds, σ_{BL}^2 and σ_{BN}^2 , propagate into the total error in the aerosol scattering ratio calculation in the same way as for the water-vapor mixing ratio calculation.

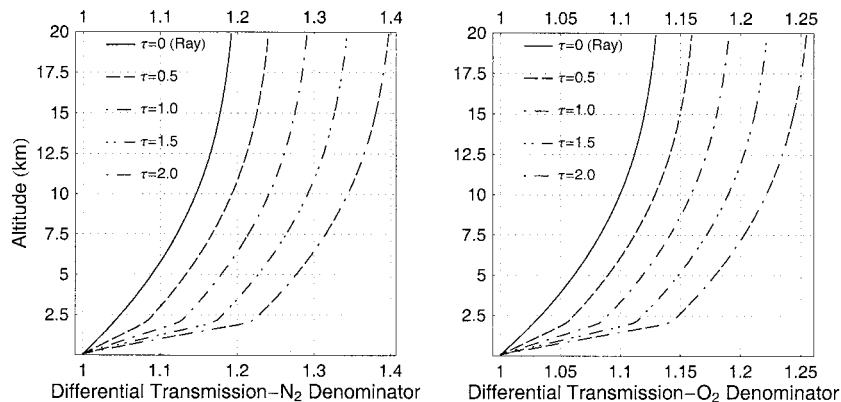


Fig. 6. DT profiles required for the aerosol scattering ratio with either Raman N_2 (left) or O_2 (right) for a range of optical depths. The laser wavelength simulated is 351.1 nm. The profiles for 354.7-nm excitation are very similar. Increasing the optical depth makes the differential transmission term larger with height. $\tau = 0$ indicates pure molecular scattering; $\tau = 2.0$ would indicate very hazy conditions. The standard atmosphere has been used in calculating the molecular extinction.

E. Aerosol Scattering Ratio Differential Transmission

The DT term $\Delta\tau(\lambda_N, \lambda_L, r)$ in Eq. (28), which accounts for the fact that the return signals at λ_L and λ_N experience different attenuations on their return trips from the scattering volume, are now computed. The influence of various aerosol loadings on this calculation are studied; the same synthesized aerosol extinction profiles shown in Fig. 2 that were used for the calculation of water-vapor differential transmission are used here.

The DT functions that result from using these aerosol extinction profiles and the molecular extinction calculated with the U.S. Standard Atmosphere density profile¹⁶ are shown in Fig. 6 for the use of the XeF excimer (351-nm) or the tripled Nd:YAG (354.7-nm) laser. The DT function that pertains to the use of the Raman N_2 signal in calculation of the aerosol scattering ratio is shown at the left, and that for O_2 is shown at the right. As stated above, the use of the O_2 signal in the scattering ratio calculation has an advantage because the DT is smaller.

For a moderately turbid value of aerosol optical depth of 0.5 (at 351–355 nm), the DT term changes by less than 5% at 20 km from the pure Rayleigh value for the use of either the N_2 or the O_2 signal. However, under the extremely hazy conditions of an aerosol optical depth of 2.0, the value of the DT term increases to approximately 1.4 (1.25) at 20 km from its pure Rayleigh value of approximately 1.15 (1.12) when the Raman N_2 (O_2) signal is used in the scattering ratio calculation. The DT curves are essentially parallel to each other above 2 km, as in the case of the water-vapor calculation shown above, because the aerosols are confined to a region below 2 km in the synthetic profiles.

The value chosen for the Angstrom coefficient influences the calculation of the differential transmission term, as shown in Fig. 7 for an exciting wavelength of 351–355 nm. Varying the Angstrom coefficient over a range of 0.8–1.2 for an aerosol optical depth of 1.0 causes a 4% change in the DT term needed when the Raman N_2 signal is used in the scattering ratio calcu-

lation. Thus, under hazy conditions, a knowledge of the wavelength scaling of the aerosols present, such as can be obtained with a sunphotometer, can help to reduce the uncertainty in this term. (However, a sunphotometer yields only the column average Angstrom coefficient. A multiwavelength lidar^{36,37} can be used to quantify the Angstrom coefficient as a function of range, but this subject is beyond the scope of the present treatment, which is confined to a single output laser wavelength.)

The DT profiles for use with the doubled (~ 532 -nm) and tripled (~ 355 -nm) Nd:YAG are shown in Fig. 8 for use of both Raman N_2 (left) and O_2 (right) in the denominator. Three situations are considered: (1) a pure Rayleigh atmosphere, (2) an aerosol optical depth of 1.0 at both 355 and 532 nm, and (3) aerosol optical depths of 1.0 at 355 and 0.67 at 532 nm. The last-named example is provided as a more

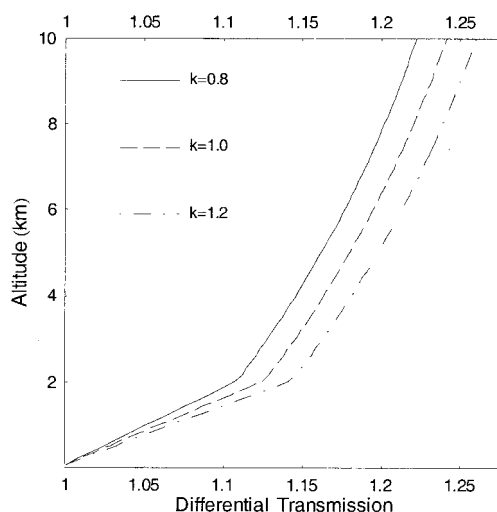


Fig. 7. Sensitivity of the aerosol scattering ratio DT profile to the wavelength scaling of aerosol extinction, assuming use of 351–355-nm excitation. For an aerosol optical depth of 1.0, the aerosol DT term is plotted for $k = 0.8, 1.0, 1.2$. The DT term changes by approximately 4% over this range.

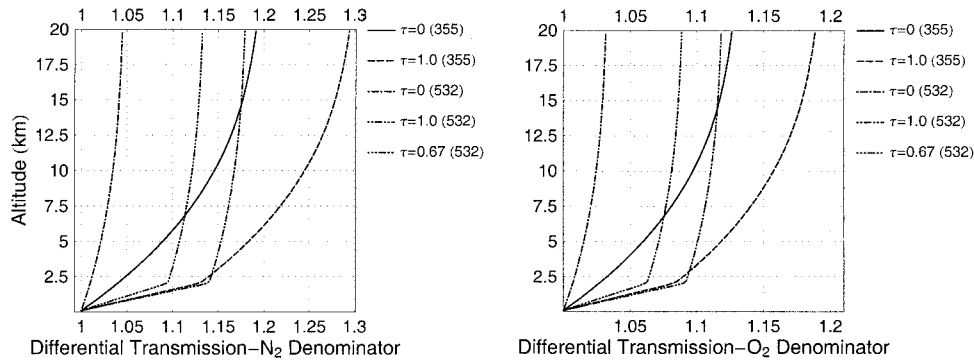


Fig. 8. DT profiles for the aerosol scattering ratio calculation with either the doubled (~ 532 -nm) or the tripled (~ 355 -nm) Nd:YAG laser. The atmospheric conditions considered are pure Rayleigh, an aerosol optical thickness of 1.0, and an aerosol optical thickness of 0.67 at 532 nm. This last-named case simulates measurements at the two laser wavelengths under similar atmospheric conditions. For the cases shown, differential aerosol extinction is responsible for more of the total DT at 532 nm than is the differential molecular extinction.

realistic comparison of the DT profile for the two laser sources operated under the same atmospheric conditions. The advantage of the Raman O_2 signal for the aerosol scattering ratio is again clear. As a general statement, the DT when O_2 is used in the denominator is approximately 60% of the value when N_2 is used. For either O_2 or N_2 the DT for a pure Rayleigh atmosphere is much less for the doubled Nd:YAG (~ 532 nm) than for the tripled Nd:YAG (~ 355 nm) (less DT means that the values are closer to 1.0). When aerosol loading is considered, the DT within the aerosol regions is more similar between the two output wavelengths than in the aerosol-free atmosphere. For $\tau = 1.0$, with either O_2 or N_2 in the denominator, the DT within the first 2 km is actually larger for the 532-nm output than for the 355-nm output. This is so because of the larger wavelength separation of the Rayleigh-Mie and Raman N_2 (or O_2) wavelengths when they are excited at 532 nm than at 355 nm and the assumption in these plots that aerosol scattering scales as λ^{-1} whereas molecular scattering scales approximately as λ^{-4} . However, a value of aerosol optical depth of 0.67 at 532 nm is consistent with an aerosol optical thickness of 1.0 at 355 nm and an Angstrom coefficient of 1.0. The use of $\tau = 0.67$ at 532 nm yields slightly smaller DT values when using $\tau = 1.0$ at 355 nm.

F. Atmospheric Calibration of the Aerosol Scattering Ratio

The atmosphere offers a natural calibration tool for determining the factor $C_{N,O}^*(\lambda_L, r)$ in Eq. (28). Russell *et al.*^{38,39} demonstrated that, in nonvolcanic conditions and in the absence of desert dust or clouds, there are few aerosols present in the free troposphere (above the boundary layer but below the tropopause). They showed that the minimum value of aerosol scattering ratio $\mathcal{R}_{\min}(\lambda)$ for a wavelength of 690 nm is not greater than 1.02. Using this value of $\mathcal{R}_{\min}(\lambda)$ and a λ^{-4} dependence for Rayleigh scattering and assuming a λ^{-k} dependence in aerosol scattering coefficient (considered constant as a function of range) imply

that the correct value of $\mathcal{R}_{\min}(\lambda)$ can be determined in the following manner.

The wavelength scaling of the Rayleigh and Mie backscattering coefficients may be expressed as

$$\frac{\beta_{\pi}^{\text{mol}}(\lambda_1, r)}{\beta_{\pi}^{\text{mol}}(\lambda_2, r)} = \left(\frac{\lambda_2}{\lambda_1}\right)^4, \quad (36)$$

$$\frac{\beta_{\pi}^{\text{aer}}(\lambda_1, r)}{\beta_{\pi}^{\text{aer}}(\lambda_2, r)} = \left(\frac{\lambda_2}{\lambda_1}\right)^k. \quad (37)$$

Given that the aerosol scattering ratio at wavelength λ_1 is

$$\mathcal{R}(\lambda_1, r) = 1 + \frac{\beta_{\pi}^{\text{aer}}(\lambda_1, r)}{\beta_{\pi}^{\text{mol}}(\lambda_1, r)}, \quad (38)$$

Eqs. (36)–(38) can now be used to scale the scattering ratio to different wavelengths. Therefore at λ_2 the following equation pertains:

$$\begin{aligned} \mathcal{R}(\lambda_2, r) &= 1 + \frac{(\lambda_1/\lambda_2)^k \beta_{\pi}^{\text{aer}}(\lambda_1, r)}{(\lambda_1/\lambda_2)^4 \beta_{\pi}^{\text{mol}}(\lambda_1, r)} \\ &= 1 + \frac{\beta_{\pi}^{\text{aer}}(\lambda_1, r)}{(\lambda_1/\lambda_2)^{4-k} \beta_{\pi}^{\text{mol}}(\lambda_1, r)}. \end{aligned} \quad (39)$$

Using now the values $\lambda_1 = 690$ nm, $\lambda_2 \equiv 350$ nm, $\mathcal{R}_{\min}(690, r) = 1.02$, and $k = 1$ yields $\mathcal{R}_{\min}(350, r) \equiv 1.003$. The Angstrom coefficient, k , generally varies between the extremes of approximately 0 and 2. Even assuming the maximum value of $k = 2$, $\mathcal{R}_{\min}(350, r) \equiv 1.005$. Because of the very small value of $\mathcal{R}_{\min}(\lambda = 350, r)$ for all values of k , one can calculate the aerosol backscattering ratio by assuming that the minimum value of backscattering ratio that a UV Raman lidar measures from 6 to 10 km corresponds to an aerosol backscattering ratio of 1.0. The error in this assumption is much less than 1%. For a visible Raman lidar operating at 532 nm, however, the appropriate normalization value is $\mathcal{R}_{\min}(532, r) \equiv 1.01$.

Although the atmosphere offers a convenient cali-

bration source for calculation of the aerosol scattering ratio, the inclusion of the temperature-sensitive functions in Eq. (28) changes this calculation significantly from what has traditionally been done with Raman lidar.^{9,13} This effect is now discussed.

1. Effect of the Temperature-Sensitivity Functions

After the DT functions are applied as shown above and $F_N(T)$ [or $F_O(T)$] and $F_R(T)$ in Eq. (28) are accounted for, $C_N^*(\lambda_L, r)$ is chosen such that the value of Eq. (28) is 1.0 in a region of the atmosphere that is free of aerosols. $F_N[T(r)]$ is a multiplicative factor implying that, in addition to changing the required calibration constant, changes in the value of F_N between the reference point (typically ~ 8 km) and where the scattering ratio calculation is being performed affect the calculated scattering ratio. For example, the use of a 75-cm^{-1} (100-cm^{-1}) width passband implies¹ that the value of $F_N(T)$ [$F_O(T)$] changes between the surface and 8 km by approximately 0.8% (1.7%), assuming a 50-K temperature difference. Inasmuch as $F_N(T)$ and $F_O(T)$ increase with height, the effect on scattering ratios measured in the boundary layer is to decrease the value compared with that derived with the traditional technique that does not account for these temperature-related changes.

The additive term $F_R(T)$ has a relatively small percentage effect on scattering ratio value \mathcal{R} . However, the aerosol backscatter coefficient is proportional to $\mathcal{R} - 1$, so relatively small values of $F_R(T)$ can have a large effect on the backscatter coefficient. The situation is quite similar to that of a high-spectral-resolution lidar in which the rotational Raman lines are excluded⁴⁰ from the measurement, and a correction must be made for the excluded part of the cross section. Both changes in the value of $F_R(T)$ with height and its absolute value affect the calculation of \mathcal{R} . For example, if an $\sim 25\text{-cm}^{-1}$ passband is used to measure the Rayleigh-Mie signal,¹ Fig. 1 indicates that the value of $F_R(T)$ is ~ 0.97 and is nearly height independent. The influence of the temperature-dependent effects on the calculation of the aerosol backscatter coefficient (to be discussed in Section 4.G) is shown in Fig. 9. The percentage error in $\beta(\lambda_L, r)$ [calculated as $(\beta_{\text{new}} - \beta_{\text{old}})/\beta_{\text{new}}$, where β_{new} includes the temperature effects and β_{old} does not] due to the exclusion of the temperature-dependent effects considered here is plotted against the aerosol-scattering ratio calculated in the traditional manner that excludes the temperature-dependent effects. The case simulated is for an $\sim 100\text{-cm}^{-1}$ -wide Raman nitrogen passband and an $\sim 25\text{-cm}^{-1}$ -wide Rayleigh-Mie passband. It is clear from the figure that the error in the aerosol backscatter coefficient increases sharply as the scattering ratio decreases. If the traditional techniques are used, the figure indicates that for a scattering ratio of 1.2 (1.1), the calculated backscatter coefficient will be $\sim 12\%$ ($\sim 25\%$) too large for this combination of passbands. This result implies that previous analyses of narrow spectral band Raman lidar measurements of aerosol backscattering have a positive bias that increases as aerosol loading de-

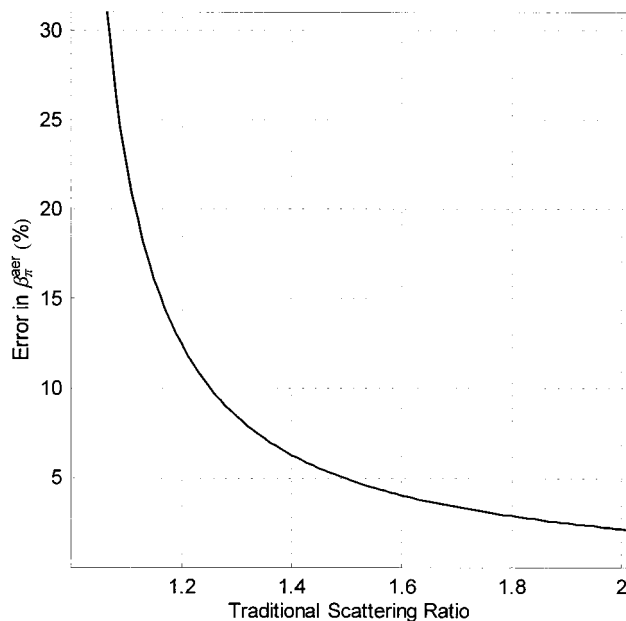


Fig. 9. Errors introduced in the calculation of the aerosol backscatter coefficient created by ignoring the temperature-dependent functions is explored here for an $\sim 100\text{-cm}^{-1}$ -wide Raman N_2 passband and an $\sim 25\text{-cm}^{-1}$ -wide Rayleigh-Mie passband. The percentage error in the backscatter coefficient is plotted against the traditional aerosol scattering ratio values. For this choice of passband widths, the error in the quantification of the aerosol backscatter coefficient exceeds 10% for all traditional scattering ratios less than ~ 1.25 . This implies that there is a positive bias to aerosol backscatter determination by use of narrowband detection if the temperature functions are not accounted for.

creases. The fractional error in the extinction-to-backscatter ratio will essentially be the same.

2. Calibration Using an Aerosol-Free Region of the Atmosphere

The determination of the aerosol scattering ratio from Eq. (28) is illustrated in Fig. 10 by use of SRL data acquired during the night of 22 August 1998 at Andros Island, Bahamas, over a 10-min period. The use of wideband filters for this measurement implies, as in the case for the water-vapor mixing ratio profile considered in Subsection 3.G, that the temperature functions have negligible effect. The quantity $F_N(r)P(\lambda_L, r)/P(\lambda_N, r) - F_R(r)$ is plotted as a solid curve. The profile slopes toward smaller values as altitude increases because of the DT of the two lidar wavelengths: 351.1 nm for aerosol and 382.3 nm for nitrogen in this example. Because of the wide spectral filters in use for these XeF excimer laser (351-nm) based measurements,^{18,25} both $F_N(r)$ and $F_R(r)$ are approximately equal to 1.0, unlike in the case of a narrow-passband system. Multiplying by the differential transmission term $\Delta\tau(\lambda_N, \lambda_L, r)$ in Eq. (28) yields the dashed curve shown. We can now determine $C_N^*(\lambda_L = 351, r)$ by normalizing the profile to a value of 1.0 in an aerosol-free value region of the atmosphere. As described above, the region from 6 to 10 km is used for this normalization. The

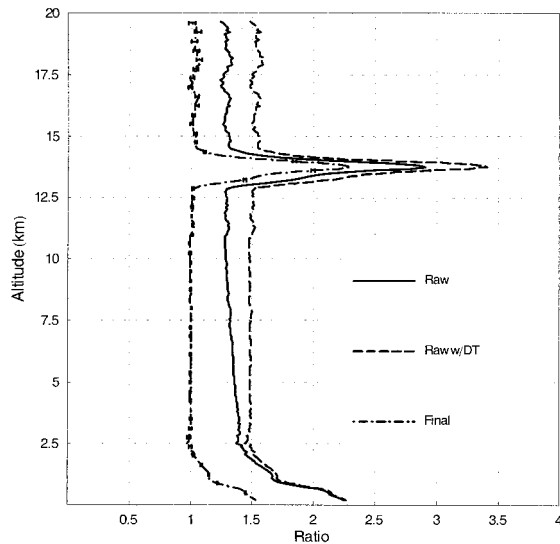


Fig. 10. Steps in the evaluation of Eq. (28) by use of data acquired by the SRL over a 10-min period on the night of 22 August 1998. The raw lidar quantity $F_N[T(r)]P(\lambda_L, r)/P(\lambda_N, r)\Delta\tau(\lambda_N, \lambda_L, r) - F_R[T(r)]$ is shown. The dashed curve is the same quantity after the first term has been multiplied by the DT profile $\Delta\tau(\lambda_N, \lambda_L, r)$ calculated from Eq. (28) from actual lidar aerosol extinction data and the molecular number density from a radiosonde. Finally the value of C_N^* as determined by normalizing the curve from 6 to 10 km, where aerosol scattering is negligible is shown. The final curve is the fully processed aerosol backscattering ratio given by $\beta_{\pi}^{\text{tot}}(\lambda_L, r)/\beta_{\pi}^R(\lambda_L, r)$. The random error in the final signal is also shown.

dashed–dotted curve then is the fully processed aerosol backscattering ratio $\beta_{\pi}^{\text{tot}}(\lambda_L, r)/\beta_{\pi}^R(\lambda_L, r)$ with errors calculated from relation (34). From the profiles, one can see small amounts of aerosol scattering present near the surface, with scattering ratios reaching ~ 1.5 . Cirrus clouds can be seen at 13–14 km, where the values are greater than 2.

From this example, $C_N^*(\lambda_L = 351, r)$ has a value of approximately 0.65 outside the overlap region. In view of Eq. (29), this value of $C_N^*(\lambda_L = 351, r)$ implies that the ratio of transmission efficiencies, $\xi(\lambda_N)/\xi(\lambda_L)$, must be of the order of 10^3 . In fact, these data were acquired with an ND3 (transmission, 10^{-3}) neutral-density filter installed in the Rayleigh–Mie channel to allow the signal to be acquired by use of photon counting electronics. This example illustrates that an absolute calibration of the aerosol scattering ratio by use of the equations outlined here and a radiometric determination of the transmission efficiency ratio of the lidar channels will be possible. The Rayleigh and Raman N_2 (or O_2) cross sections are known to better than 5% accuracy, eliminating the largest error source that is present in the similar attempt to calibrate the water-vapor mixing ratio. The aerosol backscattering coefficient can now be calculated from the aerosol scattering ratio.

G. Aerosol Backscattering Coefficient

The aerosol backscatter coefficient is easily determined from Eq. (16):

$$\beta^{\text{aer}}(\lambda_L, z) = \beta_{\pi}^{\text{mol}}(\lambda_L, z)[\mathcal{R}(\lambda_L, z) - 1]. \quad (40)$$

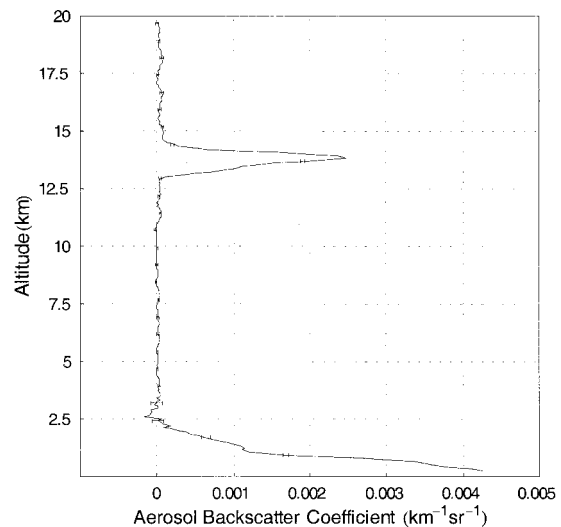


Fig. 11. Aerosol backscattering coefficient calculated on the night of 22 August 1998. Tropospheric aerosols can be seen up to altitudes of approximately 3 km, whereas a cirrus cloud layer is apparent from 13 to 15 km.

Figure 11 shows the aerosol backscatter coefficient that corresponds to the aerosol scattering ratio given in Fig. 10. The errors plotted are those that are due to the random error in the aerosol scattering ratio given by relation (34).

In terms of backscatter coefficient, which gives the intensity of light backscattered per incident photon, the tropospheric aerosols yield higher values than the cirrus cloud. In terms of the aerosol scattering ratio given in Fig. 10, however, the scattering ratio of the cloud is larger than that for the tropospheric aerosols. So, although the cirrus cloud has a lower probability of backscattering an incident photon than does the tropospheric aerosol layer, the ratio of scattering from the cirrus clouds and from molecules at the height of the cirrus cloud is greater than the corresponding ratio for the tropospheric aerosols.

H. Extinction-to-Backscatter Ratio

The ratio of aerosol extinction to backscatter is an important optical parameter that can yield information about the physical nature of aerosols. For example, quantification of this ratio is useful for the study of growth of aerosols as a function of relative humidity.¹² Aerosol backscatter data from 26 August 1998 are shown in Fig. 12. Data acquired at an angle of 10° above the horizon on that night were used to improve the vertical resolution. This entails assuming horizontal homogeneity and mapping the data acquired at an angle into the vertical, which permits retrievals of both extinction and backscattering to lower altitudes than is possible with vertical measurements only.

In general during the CAMEX-3 campaign,²³ the top of the marine boundary layer was observed to be at ~ 1 km, as indicated by a roughly constant water-vapor mixing ratio. A signature can be seen in the aerosol data at this altitude that likely indicates the

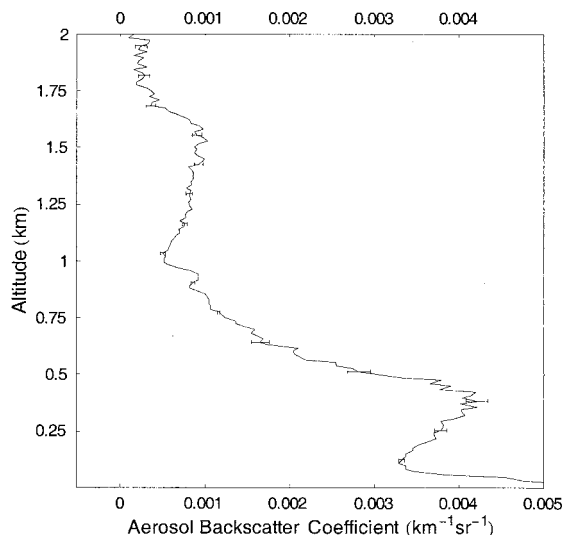


Fig. 12. Aerosol backscatter coefficient for the tropospheric aerosols that were present during the night of 26 August 1998 at Andros Island, Bahamas. Data acquired at a low elevation angle have been used to improve the measurement of extinction by conversion of the angle profile to a vertical profile by use of an assumption of horizontal homogeneity.

top of the marine boundary layer. Above this layer the backscattering that is due to aerosols increases slightly, which is consistent with a change in aerosol composition. The same signature can be seen in the extinction-to-backscatter ratio (S_a). This ratio is formed by use of the data shown in Fig. 6 of part 1 and in Fig. 12 here. The result is plotted in Fig. 13. The error bars plotted for S_a are determined from standard error propagation techniques based on the error equations for extinction and backscattering presented above. The relative decrease in S_a above 1 km is another indication of a change in aerosol type.

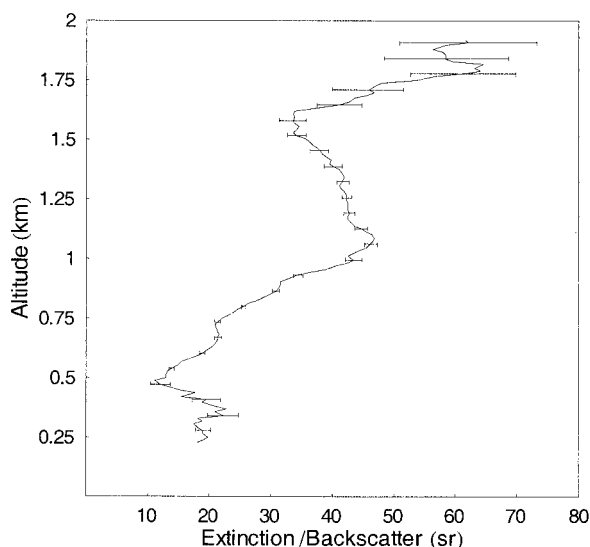


Fig. 13. Aerosol extinction-to-backscatter ratio from a summation of data for 20 min on the night of 26 August 1998 at Andros Island, Bahamas.

This could be an indication of the presence of different aerosol types that have been transported aloft from different locations rather than of local aerosols that swelled within the marine boundary layer.

The increase in extinction-to-backscatter ratio up to an altitude of 1 km, the height of the marine boundary layer, could be an indication of aerosol swelling. Such swelling is often seen as height increases inside a well-mixed boundary layer. Aerosols begin to swell when the relative humidity increases above $\sim 70\%$.⁴¹ Inasmuch as a well-mixed boundary layer should have a relatively constant mixing ratio and the mixing ratio is a conserved quantity, as a parcel of air cools within the boundary layer the relative humidity of the parcel will increase. Atmospheric temperature typically decreases with altitude; thus the relative humidity is often seen to increase with altitude in the boundary layer. When the relative humidity exceeds $\sim 70\%$, one can expect aerosol swelling to commence if the aerosol had not previously been hydrated, in which case swelling could occur at lower relative humidities. The increase in S_a from 0.5 to 1.0 km could be due to increases in relative humidity above the threshold value of 70%. In fact, measurements of atmospheric temperature made by the Atmospheric Emitted Radiance interferometer (AERI)⁴² coupled with the lidar mixing ratio measurements indicated that relative humidities exceeded 70% between approximately 0.4 and 1.1 km, supporting the conclusion that the increase in S_a between 1.0 km is due to aerosol growth.

5. Summary and Conclusions

In this paper, which is the second of a two-part analysis of the traditional Raman lidar measurements of water vapor and aerosols, the temperature-dependent forms of the lidar equations that were developed in part 1¹ have been used to derive equations for the water-vapor mixing ratio, the aerosol scattering ratio, the aerosol backscatter coefficient, and the aerosol extinction-to-backscatter ratio. The appropriate error equations were also derived for these quantities. The effect of the change of intensity of Raman rotational and vibrational-rotational lines versus temperature were simulated by use of Gaussian functions for different passband widths. The current ability to model the Rayleigh, Raman water vapor, N_2 , and O_2 spectra accurately, coupled with accurate measurements of lidar system transmission characteristics made with a calibration lamp, imply that absolute calibration of both water vapor and aerosol backscattering measurements is possible. An accurate water-vapor calibration will require improved knowledge of the ratio of Raman N_2 and water-vapor cross sections, although that may be achievable by careful calibration of the U.S. Department of Energy Raman lidar system. An accurate absolute calibration of aerosol backscattering should be possible now.

It was shown that the use of narrowband detection for the water-vapor mixing ratio can change the calculation of water-vapor mixing ratio by 5% and more

for upper tropospheric measurements, whereas for an aerosol scattering ratio the effects can exceed 10% for light aerosol conditions with slightly larger effects found for aerosols confined to the atmospheric boundary layer. This implies that previous analyses of Raman lidar water-vapor and aerosol data may be in error by significant amounts because of these narrow passband effects. This probability has potential implications for the use of Raman lidar in quantifying upper tropospheric water vapor, such as has been done with both the NASA Goddard Space Flight Center Scanning Raman Lidar and the U.S. Department of Energy's Cloud and Radiation Testbed Raman lidar. Measurements of the transmission characteristics of narrow-passband Raman water-vapor lidar channels are needed with accuracies of ~ 0.1 Å to ensure that the temperature corrections developed here can be applied with confidence. Such high accuracies are not required for the Rayleigh-Mie, Raman N_2 , and O_2 channels due to the symmetric nature of the spectra involved. The influence of temperature dependence of Raman scattering has perhaps a larger effect on the traditional calculations of aerosol backscatter coefficient and extinction-to-backscatter ratio.

The results developed here indicate that a positive bias will exist in the aerosol backscatter coefficient measured by use of narrowband detection and that the effect becomes quite large for light aerosol loading. This implies that previous calculations of aerosol scattering properties measured with a narrow band Raman lidar may need to be revised. For a given passband width, this effect increases for smaller values of backscattering. A positive bias in backscattering implies that the extinction-to-backscatter ratios are correspondingly too low by a similar amount, with the effect again increasing as aerosol loading decreases.

The same implications are present in quantifying S_a in thin cirrus clouds. Previous analyses of cirrus cloud S_a based on narrow-passband measurements will exhibit a positive bias in the backscatter coefficient that increases as cloud backscatter decreases. This implies that the database of Raman lidar thin cirrus cloud S_a measurements acquired by use of narrowband detection is increasingly biased toward lower values of S_a as cirrus optical depth decreases.

There is every expectation that Raman lidar will continue to be one of the most powerful remote-sensing tools for studying the atmosphere. As the Raman lidar technique moves increasingly into daytime and upper tropospheric measurements, the use of narrowband detection will increase. The results presented here indicate that the basic analytical techniques used to calculate the traditional Raman lidar quantities of water-vapor mixing ratio, aerosol scattering ratio, aerosol backscatter coefficient, and extinction-to-backscatter ratio therefore require modification. The temperature-dependent functions required for the analysis of data from a particular lidar system can be calculated upon request.

Support for this activity has come from the NASA Radiation Sciences and Dynamics and Remote Sensing Program as well as the U.S. Department of Energy's Atmospheric Radiation Measurements program.

References and Notes

1. D. N. Whiteman, "Examination of the traditional Raman lidar technique. I. Evaluating the temperature-dependent lidar equations," *Appl. Opt.* **42**, 2571–2592 (2003).
2. A. T. Young, "Revised depolarization corrections for atmospheric extinction," *Appl. Opt.* **19**, 3427–3428 (1980).
3. A. T. Young, "On the Rayleigh-scattering optical depth of the atmosphere," *J. Appl. Meteorol.* **20**, 328–330 (1980).
4. Lord Rayleigh, "On the light from the sky, its polarization and color," *Phil. Mag.* **41**, 107–120, 274–279 (1871).
5. Lord Rayleigh, "On the scattering of light by small particles," *Phil. Mag.* **41**, 447–454 (1871).
6. M. Born and E. Wolf, *Principles of Optics* (Cambridge U. Press, Cambridge, 1999).
7. C. F. Bohren and B. A. Albrecht, *Atmospheric Thermodynamics* (Oxford U. Press, New York, 1998).
8. G. Vaughan, D. P. Wareing, L. Thomas, and V. Mitev, "Humidity measurements in the free troposphere using Raman backscatter," *Q. J. R. Meteorol. Soc.* **114**, 1471–1484 (1988).
9. D. N. Whiteman, S. H. Melfi, and R. A. Ferrare, "Raman lidar system for the measurement of water vapor and aerosols in the Earth's atmosphere," *Appl. Opt.* **31**, 3068–3082 (1992).
10. U. Wandinger and A. Ansmann, "Experimental determination of the lidar overlap profile with Raman lidar," *Appl. Opt.* **41**, 511–514 (2002).
11. M. Bass, ed., *Handbook of Optics* (McGraw-Hill, New York, 1995).
12. R. A. Ferrare, S. H. Melfi, D. N. Whiteman, K. D. Evans, and R. Leifer, "Raman lidar measurements of aerosol extinction and backscattering. 1. Methods and comparisons," *J. Geo. Phys. Res.* **103**, 19663–19672 (1998).
13. A. Ansmann, M. Riebesell, C. Weitkamp, E. Voss, W. Lahmann, and W. Michaelis, "Combined Raman elastic-backscatter lidar for vertical profiling of moisture, aerosol extinction, backscatter, and lidar ratio," *Appl. Phys. B.* **55**, 18–28 (1992).
14. D. D. Turner and J. E. M. Goldsmith, "Twenty-four-hour Raman lidar water vapor measurements during the Atmospheric Radiation Measurement program's 1996 and 1997 water vapor intensive observation periods," *J. Atmos. Ocean. Tech.* **16**, 1062–1076 (1999).
15. R. M. Measures, *Laser Remote Sensing Fundamentals and Applications* (Wiley-Interscience, New York, 1984).
16. *U.S. Standard Atmosphere*, NOAA document S/T 76-1562 (National Oceanic and Atmospheric Administration, National Aeronautics and Space Administration, U.S. Air Force, Washington, D.C., 1976).
17. J. E. M. Goldsmith, F. H. Blair, S. E. Bisson, and D. D. Turner, "Turn-key Raman lidar for profiling atmospheric water vapor, clouds, and aerosols," *Appl. Opt.* **37**, 4979–4990 (1998).
18. D. N. Whiteman and S. H. Melfi, "Cloud liquid water, mean droplet radius and number density measurements using a Raman lidar," *J. Geophys. Res.* **104**, 31411–31419 (1999).
19. P. R. Bevington and D. K. Robinson, *Data Reduction and Error Analysis for the Physical Sciences* (McGraw-Hill, New York, 1992).
20. D. N. Whiteman, G. Schwemmer, T. Berkoff, H. Plotkin, L. Ramos-Izquierdo, and G. Pappalardo, "Performance modeling of an airborne Raman water-vapor lidar," *Appl. Opt.* **40**, 375–390 (2001).
21. R. A. Ferrare, S. H. Melfi, D. N. Whiteman, K. D. Evans, F. J.

- Schmidlin, and D. O'C. Starr, "A comparison of water vapor measurements made by Raman lidar and radiosondes," *J. Atmos. Ocean. Tech.* **12**, 1177–1195 (1995).
22. Modtran 4 Radiative Transfer Code (U.S. Air Force Research Lab, Space Vehicles Directorate, Hanscom Air Force Base, Mass., 1999).
 23. D. N. Whiteman, K. D. Evans, B. Demoz, D. O'C. Starr, D. Tobin, W. Feltz, G. J. Jedlovec, S. I. Gutman, G. K. Schwemmer, M. Cadirola, S. H. Melfi, and F. J. Schmidlin, "Raman lidar measurements of water vapor and cirrus clouds during the passage of hurricane Bonnie," *J. Geophys. Res.* **106**, 5211–5225 (2001).
 24. V. Sherlock, A. Hauchecorne, and J. Lenoble, "Methodology for the independent calibration of Raman backscatter water-vapor lidar systems," *Appl. Opt.* **38**, 5816–5837 (1999).
 25. D. N. Whiteman, W. F. Murphy, N. W. Walsh, and K. D. Evans, "Temperature sensitivity of an atmospheric Raman lidar system based on a XeF excimer laser," *Opt. Lett.* **18**, 247–249 (1993).
 26. E. R. Miller, J. Wang, and H. L. Cole, "Correction for dry bias in Vaisala radiosonde RH data," presented at the Ninth ARM Science Team Meeting, San Antonio, Texas, 22–26 March 1999.
 27. B. M. Lesht, "Reanalysis of radiosonde data from the 1996 and 1997 Water Vapor Intensive Operations Periods: applications of the Vaisala RS-80H contamination correction algorithm to dual-sonde soundings," presented at the Ninth ARM Science Team Meeting, San Antonio, Texas, 22–26 March 1999.
 28. B. M. Lescht, "Uncertainty in radiosonde measurements of temperature and relative humidity estimated from dual-sonde sounds made during the September 1996 ARM Water Vapor IOP," in *Proceedings of the 10th Symposium on Meteorological Observations and Instrumentation* (American Meteorological Society, Dallas, Texas, 1998), pp. 80–83.
 29. D. N. Whiteman, T. Berkoff, D. D. Turner, T. Tooman, R. Ferrare, and L. Heilman, "Research efforts in the absolute calibration of a Raman water vapor lidar," presented at the 20th International Laser Radar Conference, Vichy, France, 10–14 July 2000.
 30. C. M. Penney and M. Lapp, "Raman-scattering cross-section for water vapor," *J. Opt. Soc. Am.* **66**, 422–425 (1976).
 31. G. Avila, J. M. Fernandez, B. Mate, G. Tejeda, and S. Montero, "Ro-vibrational Raman cross sections of water vapor in the OH stretching region," *J. Mol. Spectrosc.* **196**, 77–92 (1999).
 32. G. Herzberg, *Spectra of Diatomic Molecules*, Vol. 1 of Molecular Spectra and Molecular Structure (Kreiger, Malabar, Fla., 1989).
 33. C. M. Penney, R. L. St. Peters, and M. Lapp, "Absolute rotational Raman cross sections for N₂, O₂, CO₂," *J. Opt. Soc. Am.* **64**, 712–716 (1976).
 34. W. S. Heaps, J. Burris, and J. A. French, "Lidar technique for remote measurement of temperature by use of vibrational-rotational Raman spectroscopy," *Appl. Opt.* **36**, 9402–9405 (1997).
 35. A. Clough, Atmospheric and Environmental Research, Inc., 131 Hartwell Avenue, Lexington, Mass. (personal communication, 2002).
 36. D. Muller, K. Franke, F. Wagner, D. Althausen, A. Ansmann, and J. Heintzenberg, "Vertical profiling of optical and physical particle properties over the tropical Indian Ocean with six-wavelength lidar. 1. Seasonal cycle," *J. Geophys. Res.* **106**, 28567–28575 (2001).
 37. D. Muller, K. Franke, F. Wagner, D. Althausen, A. Ansmann, J. Heintzenberg, and G. Verver, "Vertical profiling of optical and physical particle properties over the tropical Indian Ocean with six-wavelength lidar. 2. Case studies," *J. Geophys. Res.* **106**, 28577–28595 (2001).
 38. P. B. Russell, T. J. Swissler, and M. P. McCormick, "Methodology for error analysis and simulation of lidar measurements," *Appl. Opt.* **18**, 3783–3797 (1979).
 39. P. B. Russell, B. M. Morley, J. M. Livingston, G. W. Grams, and E. M. Patterson, "Orbiting lidar simulations. 1. Aerosol and cloud measurements by an independent-wavelength technique," *Appl. Opt.* **21**, 1541–1553 (1982).
 40. C.-Y. She, "Spectral structure of laser light scattering revisited: bandwidths of nonresonant scattering lidars," *Appl. Opt.* **40**, 4875–4884 (2001).
 41. A. Deepak and L. H. Ruhnke, *Hygroscopic Aerosols* (Deepak, Hampton, Va., 1984).
 42. W. F. Feltz, W. L. Smith, R. O. Knuteson, H. E. Revercomb, H. M. Woolf, and H. B. Howell, "Meteorological applications of temperature and water vapor retrievals from the ground-based Atmospheric Emitted Radiance Interferometer (AERI)," *J. Appl. Meteorol.* **37**, 857–875 (1998).